



UvA-DARE (Digital Academic Repository)

A spectral-timing approach to the study of AGN outflows

de Jesus Silva, C.V.

Publication date

2018

Document Version

Other version

License

Other

[Link to publication](#)

Citation for published version (APA):

de Jesus Silva, C. V. (2018). *A spectral-timing approach to the study of AGN outflows*. [Thesis, fully internal, Universiteit van Amsterdam].

General rights

It is not permitted to download or to forward/distribute the text or part of it without the consent of the author(s) and/or copyright holder(s), other than for strictly personal, individual use, unless the work is under an open content license (like Creative Commons).

Disclaimer/Complaints regulations

If you believe that digital publication of certain material infringes any of your rights or (privacy) interests, please let the Library know, stating your reasons. In case of a legitimate complaint, the Library will make the material inaccessible and/or remove it from the website. Please Ask the Library: <https://uba.uva.nl/en/contact>, or a letter to: Library of the University of Amsterdam, Secretariat, Singel 425, 1012 WP Amsterdam, The Netherlands. You will be contacted as soon as possible.

Constraining the physical properties of the UV ionized absorber in NGC 5548 with time-dependent photoionization modeling

C.V. Silva, G.A. Kriss, E. Costantini, P. Uttley et al.

To be submitted to Astronomy & Astrophysics

Abstract

A comprehensive reverberation monitoring campaign was conducted on NGC 5548 during ~ 6 months, in the first half of 2014. The retrieved UV data with the Cosmic Origins Spectrograph on HST at intervals of ~ 1 day allowed for the variability of the intrinsic narrow absorption lines to be uncovered in great detail. Equivalent width measurements for the observed troughs as a function of time were obtained. The time-dependent behaviour of the troughs is well correlated with the ionizing flux suggesting that the gas is responding to changes in the central source. These high-quality data thus provide a unique opportunity to test time-dependent photoionization models. Here, we expand on the time-dependent photoionization model we developed in previous work for the study of X-ray warm absorbers, and numerically compute the predicted ion concentrations as a function of time reacting to the intrinsic variations of the illuminating continuum, for a grid of gas densities and ionization states. In the optically thin limit, and assuming a fixed total column-density, the ion concentrations show a linear correlation with the measured equivalent widths, allowing us to directly compare the predicted time-dependent behaviour of the gas to the observed equivalent width light curves. By fitting the data with our time-dependent models, we successfully constrain both the density and ionization parameter of two of the six

velocity components of the gas. Our results highlight the validity and importance of time-dependent photoionization models for the characterization of AGN outflows.

3.1 Introduction

Active Galactic Nuclei (AGN) outflows can be powerful enough to play a role in the evolution of the host galaxy. The energy and matter expelled from the nucleus are able to interact with the surrounding environment, a phenomenon known as AGN feedback (e.g. Di Matteo et al. 2005; Hardcastle et al. 2007; King & Pounds 2015). Characterizing the outflows is hence crucial information for the understanding of the inner most regions of active galaxies and the interaction of the supermassive black hole with its surroundings.

In Seyfert galaxies, the outflow is detected through the presence of intrinsic absorption features in their UV and X-ray spectra, which are blueshifted with respect to the systemic velocity of the galaxy (see Crenshaw et al. 2003a, for a review). The origin and driving mechanisms of these outflows are still up for debate, and assessing their importance for feedback has been proven to be all but trivial (e.g. Crenshaw & Kraemer 2012). One of the main problems associated with the latter challenge relates to the estimation of the distance between the supermassive black hole and the absorbing gas, which can then be used to quantify the momentum transferred by the outflow into the surrounding medium. Characterizing the location of the absorber is possible if a density estimate for the gas can be made. In the UV, density-sensitive lines from metastable levels can be used to directly infer the density. This method has successfully been applied to some sources (e.g. Arav et al. 2015), yet in many cases such diagnostic lines are simply not detected. Furthermore, the sensitivity of the metastable absorption lines to density diagnostics is dependent on the ionization of the gas, implying that different lines are only able to probe a certain range of densities (Mao et al. 2017). Another method to estimate this quantity is by studying the variability. The outflowing gas, ionized by the central source, is subjected to variations of the ionizing flux, typically observed in AGN. The response time of the gas to such changes in flux, i.e. the time the gas takes to reach photoionization equilibrium with the ionizing continuum, is inversely proportional to the density (e.g. Krolik & Kriss 1995; Bottorff et al. 2000). Thus detailed monitoring of these systems can be a powerful method to constrain the location of the gas relative to the central source. In the X-rays, Nicastro et al. (1999) applied this method to constrain the density and location of the warm absorber in NGC 4051. More recently, Kaastra et al. (2012) used a time-dependent photoionization model to constrain the distance of the dominant X-ray outflow components in Mrk 509, by comparing the predicted time-dependent transmission spectra with the observations. Making use of the ~ 600 ks of XMM-*Newton* archival observations of NGC 4051, Silva et al. (2016) performed a detailed study of the time-behaviour of the warm absorber components in this source by predicting the response of the gas to the rapid changes in the continuum, which for the first time revealed that a time delay associated with the response time of the gas due to time-dependent photoionization effects could be detected in

the lag-frequency spectra of these sources. In the X-rays, detailed monitoring of a source covering such short timescales is possible, however, such rapid variations in the absorption features are particularly hard to track with current instrumentation since we lack the resolution and signal-to-noise ratio necessary to observe these changes. Contrarily, in the UV observed changes in the absorption troughs are not uncommon. Gabel et al. (2005) was able to reproduce the observed changes in one of the UV outflow components in NGC 3783, and derive upper limits on the distances of the remaining two, through time-dependent solutions of the absorber variability based on the observed flux variations. This method also proved successful when applied to Mrk 509, where the distances of five ionization components could be derived (Arav et al. 2012) through time-dependent photoionization calculations with a set of simulated lightcurves which were then compared to the variations in the troughs. Thus it is clear that deep observations of these sources are necessary to track in detail both the changes in the ionizing continuum and the gas response.

Between May 2013 and July 2014 NGC 5548 was extensively monitored, in what is one of the most comprehensive multi-wavelength spectroscopy campaigns to date targeting an AGN (Kaastra et al. 2014a). NGC 5548 is an archetypal Seyfert 1 galaxy ($z=0.017175$, de Vaucouleurs et al. 1991), with a persistent ionized outflow detected both in the UV (see e.g. Crenshaw et al. 2003b) and X-ray bands (see e.g. Steenbrugge et al. 2005). The absorber shows evidence for six kinematic components, labelled 1 to 6 in descending order of velocity (Crenshaw et al. 2003b). Surprisingly, during the 2013-2014 campaign, the ionization of the long-lived outflow was much lower compared to previous epochs, due to the presence of obscuring matter blocking the central source which resulted in a significant decrease of the ionizing flux incident on gas at larger distances (Kaastra et al. 2014a). The obscuration event allowed for a comprehensive study of the gas, through the newly discovered absorption troughs at lower ionization due to the low incident flux level. Arav et al. (2015) found the gas variability throughout the years could be fully explained by a simple photoionization model and placed tight constraints on the distance of component 1 and useful limits on the remaining five kinematic components.

In this work, we expand the time-dependent photoionization model developed by Silva et al. (2016) to predict the variations in the ionic column densities of the UV absorbing gas, in response to changes in the ionizing continuum, for a grid of gas densities. We then estimate the density, and hence the distance, of the outflow components by directly comparing the predicted ionic column densities to the measured equivalent widths, as a function of time. By fitting our model to the equivalent width lightcurves, we are able to constrain the density, and ionization state, of components 1 and 3, and place tight constraints on the distance of these components from the central source.

The paper is structured as follows. In section 3.2, we describe the UV observations taken during the 2014 reverberation mapping campaign on NGC 5548 (De Rosa et al.

2015), the reduction of these data and its analysis to retrieve measurements of the equivalent widths of the narrow absorption lines. In section 3.3, we introduce the time-dependent photoionization model and explain how the predicted ion concentrations are calculated. In section 3.4, we fit the predicted ion concentrations to the measured equivalent widths in an attempt to constrain the density, and in addition the ionization state, of the different gas phases. Our results are discussed in section 3.5 and the conclusions are presented in section 3.6.

For consistency with the previous works, we refer to the six UV-band kinematic components of the NGC 5548 ionized absorber following the labeling mentioned earlier, adopted by Crenshaw et al. (2003b) and also implemented in Arav et al. (2015).

3.2 Observations and Data Analysis

The data used in this paper was obtained during the 6-month reverberation monitoring campaign conducted on NGC 5548 in the first half of 2014, the AGN Space Telescope and Optical Reverberation Mapping (AGN STORM) Project. Using the Cosmic Origins Spectrograph (COS; Green et al. 2012) on HST (Program ID 13330, PI B. Peterson), De Rosa et al. (2015) obtained 171 UV spectra at approximately 1-day cadence from February 1, 2014, through July 27, 2014. Gratings G130M and G160M were used to obtain spectra covering the 1153 Å–1796 Å wavelength range in four separate exposures during a single-orbit visit for each spectrum. These separate exposures were recalibrated and merged into a single spectrum for each observation as described by De Rosa et al. (2015). For wavelengths in the G130M spectral range ($\lambda < 1430\text{\AA}$), a precision of 1.1% in flux was achieved; at longer wavelengths covered by the G160M grating, precision was slightly worse at 1.4%. Custom-generated flat-fields enabled signal-to-noise ratios (S/N) of ~ 80 per pixel, although individual observations are count-rate limited to $S/N \sim 10\text{--}20$.

To measure the strengths of the individual absorption lines in each observation, an emission model was first developed for the mean NGC 5548 spectrum. This model is described in more detail by Kaastra et al. (2014a) and De Rosa et al. (2015). The model essentially consists of a power-law continuum, reddened by foreground Milky Way extinction with $E(B-V)=0.017$, with superposed emission lines. The emission lines range in complexity from single Gaussians (e.g., for a weak line such as C II $\lambda 1335$), to as many as seven Gaussian components for bright lines with two multiplets, like C IV $\lambda 1548, 1550$. In the latter case, each multiplet is described by a narrow component with full-width-at-half-maximum (FWHM) of $\sim 300\text{ km s}^{-1}$, an intermediate-width component with $\text{FWHM} \sim 800\text{ km s}^{-1}$, and a broad component with $\text{FWHM} \sim 3000\text{ km s}^{-1}$. A single very broad component (since the doublet is not resolved at such widths) of $\text{FWHM} \sim 8000\text{ km s}^{-1}$ completes the C IV profile. Similar profiles are used for Ly α , N V, He II, and Si IV.

As reported by Kaastra et al. (2014a), NGC 5548 has entered a long-lived phase where obscuring material is absorbing the soft X-ray spectrum as well as producing broad absorption troughs on the blue wings of UV resonant lines, most prominently Ly α , N V, Si IV, and C IV. The emission model for NGC 5548 also includes a description of these components, which are modeled as asymmetric Gaussians in negative flux, with the blue half of the profile having a FWHM of ~ 1000 km s $^{-1}$. Finally, the whole spectrum is absorbed by foreground Milky Way Ly α with a damped, Lorentzian profile normalized to an H I column density of 1.45×10^{20} cm $^{-2}$ s (Wakker et al. 2011).

Given this basic template developed for the mean spectrum, Kriss et al. (in prep.) describe how this model is then fit to each single observation of the NGC 5548 campaign. Fits are obtained by only using wavelengths unaffected by either foreground interstellar absorption lines or the narrow absorption lines intrinsic to NGC 5548. Starting with a spectrum near the center of the campaign with approximately the same flux as the mean spectrum, the model parameters are adjusted to provide the best fit to that individual observation. Later and earlier observations are then individually fit, in order, so that the model parameters gradually adjust and evolve with the changing shape of the spectrum during the campaign.

Once this final set of emission models for each individual observation are in hand, we can measure the equivalent widths of the individual narrow absorption lines in each spectrum. The emission model specifies the continuum level in the region of each absorption line. We obtain equivalent widths by integrating the difference between the emission model and the observed spectrum in the region spanned by each absorption line. These integrations are actually discrete pixel-by-pixel sums:

$$EW = \sum (F_i - f_i) \times (\lambda_{i+1} - \lambda_i) / f_i$$

where F_i is the observed spectrum in pixel i , f_i is the emission model value in pixel i , and λ_i is the central wavelength of each pixel. In practice, $\Delta\lambda = \lambda_{i+1} - \lambda_i$ is a constant for each pixel in the linearized combined spectrum produced for each observation.

Errors on the equivalent width are determined using straightforward propagation of the observational errors for each pixel:

$$\sigma_{EW} = \sqrt{(\sum \sigma_i^2 \times \Delta\lambda^2 / f_i^2)}$$

This process is used to extract the measurements of all the absorption lines used in this paper.

3.3 Time-dependent photoionization

The outflowing gas, responsible for the observed narrow absorption lines in the AGN UV spectra, is photoionized by the central source. In addition, the AGN continuum emission is known to be variable. As such, time-dependent effects must be considered in photoionization modeling since the fluctuations in the luminosity of the source will have an impact on the ionization balance of the gas. A decrease in the luminosity of the ionizing continuum will result in a lower ionization state of the gas. On the contrary, when the luminosity increases, the gas becomes more ionized. The processes here enabling the gas to reach equilibrium with the underlying continuum are photoionization and its inverse process, radiative recombination.

Depending on the amplitude of the flux variations the gas is exposed to and on the characteristics of the gas itself such as its density, the response to the changes in the central source may vary (Krolik & Kriss 1995). When variations in the ionizing flux occur on much longer timescales than the typical response timescale of the gas, the gas is in equilibrium with the ionizing source at all times. On the other hand, when changes in flux occur on much shorter timescales than the response timescale of the gas, the ionic abundances reach a steady state determined by the average flux. Finally, when the source's variability timescale is on the order of the response timescale of the gas, the ionic abundances show a smooth and delayed version of the flux history of the central source.

A time-dependent photoionization model that tracks the rapid changes in the ionizing continuum and predicts the relative ion concentrations as a function of time, for a grid of gas densities, was developed in previous work by Silva et al. (2016), while studying the X-ray warm absorber in NGC 4051. Here we expand on the work of Silva et al. (2016) and investigate in detail how the UV absorbing gas in NGC 5548 reacts to changes in the ionizing flux. The time behavior of the gas can be described by the time-dependent ionization balance equations as given by Krolik & Kriss (1995)

$$\frac{dn_{X^i}}{dt} = -n_{X^i}n_e\alpha_{\text{rec},X^{i-1}} - n_{X^i}I_{X^i} + n_{X^{i+1}}n_e\alpha_{\text{rec},X^i} + n_{X^{i-1}}I_{X^{i-1}}, \quad (3.1)$$

where n_e is the electron density of the gas, α_{rec,X^i} is the recombination coefficient from stage $i+1$ to i and I_{X^i} is the ionization rate from stage i to stage $i+1$. In equation 3.1, the usually small effects from Auger ionization, collisional ionization, and three-body recombination are neglected. Changes in ion concentrations, predicted through this method, are therefore influenced by the destruction rate and formation rate of each ion solely due to photoionization and radiative recombination.

Variations in the ionic concentrations induced by the flux variability are expected to influence the observed equivalent widths of the narrow absorption lines. During the extensive 6-month monitoring of NGC 5548, the narrow absorption lines appear

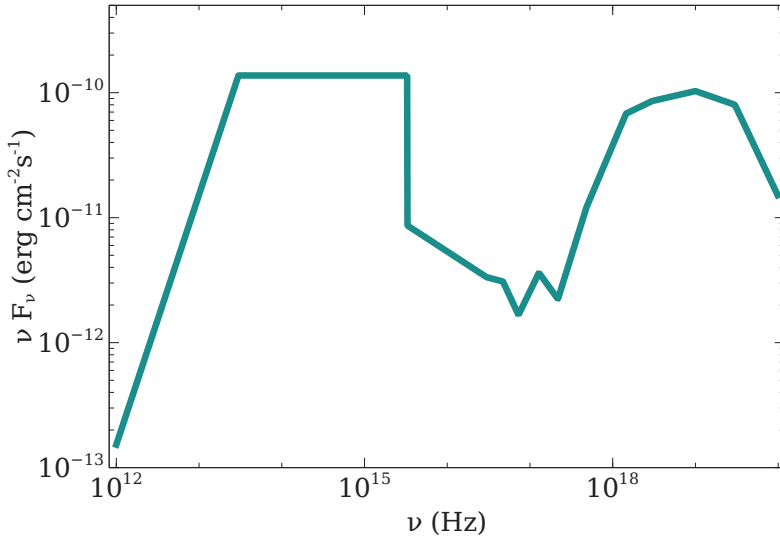


Figure 3.1: Spectral energy distribution of NGC 5548 during the obscuration event.

to be responding to changes in the continuum only throughout the first two continuum peaks (roughly corresponding to the first 60 days of observations, in which the equivalent widths are well correlated with the ionizing flux. For the second half of the campaign, an anomalous behavior of the broad UV emission lines was observed (Goad et al. 2016), suggesting that the underlying SED had changed during this period (Mathur et al. 2017). The narrow absorption lines are also affected during this anomalous epoch and a correlation with the continuum is no longer seen. For this reason, we only consider the first part of the observations in our analysis. During this time, the narrow absorption lines show the classic behavior expected from photoionization and the ionizing flux is well tracked by the far-UV continuum flux at 1367Å, providing ideal conditions to test our method. We therefore consider the flux variations at 1367Å as a proxy for the changes in the underlying continuum driving the ionization state of the gas.

3.3.1 Spectral energy distribution

The incident spectral energy distribution used throughout this work (see Fig. 3.1) is the same obscured SED adopted in Arav et al. (2015). The shape of this SED is derived from the simultaneous X-ray/UV observations from 2002 (Steenbrugge et al. 2005), modified to include the effects of the obscurer detected in the 2013 observations, which absorbed much of the soft ionizing continuum before it reached the UV outflow.

The corresponding spectral energy distribution, as well as the equilibrium ion concentrations, are essential to estimate the ionization and recombination rates. Also the ionization of the gas is a crucial parameter in these calculations. Using this SED and the latest version of CLOUDY (v.17.00, Ferland et al. 2017), we derive the relation between the ionization parameter ξ and U to be $\log(U) = \log(\xi) - 2.19$. From the six outflow components detected in the absorption spectra of NGC 5548, component 1 is the strongest and highest velocity component ($v_{\text{out}} \sim 1160 \text{ km s}^{-1}$). Arav et al. (2015) derived the average ionization parameter of this component to be $\log U \sim -1.5$. Since for the other components the estimates on the ionization parameter are rather loose or non-existent, we start this analysis by considering only component 1. For the following computations we use the corresponding ionization parameter, $\log \xi \sim 0.69$, for this component. These results are later presented in Sec. 3.4.1. The remaining components are analysed in Sec. 3.4.2, where we simultaneously constrain the ionization and density of the gas. In this case, the ionization and recombination rates were computed in a similar fashion as described below, though for a grid of ξ .

3.3.2 Ionization and recombination rates

The ionization and recombination rates were calculated with CLOUDY, for each point in the light curve, using the SED from Fig. 3.1 and assuming proto-Solar abundances (Lodders et al. 2009). We make use of the command "print rates" to retrieve the ionization and recombination rates for each ion, for the different flux levels by feeding CLOUDY with the appropriate scaled ionization parameter, such that it matches the luminosity changes during the observation. The assumption here is that the density and distance of the gas to the central source remain constant for these short timescales. In this way, the average ionization parameter, $\xi \sim 0.69$, can be linearly scaled up or down with the changes in the luminosity, according to the relation $\xi = L_{\text{ion}}/nr^2$. Since CLOUDY includes multiple ionization after inner-shell ionization and in equation 3.1 multiple ionization is not taken into account, we correct the ionization rates to force equilibrium when inserting these in equation 3.1 with the equilibrium concentrations, which needs to yield $dn_{X^i}/dt = 0$.

3.3.3 Time-dependent ion concentrations

The time-dependent ion concentrations are calculated by integrating the ionization balance equations (see equation 3.1). These form a system of N-coupled ordinary differential equations that we solve numerically by using the subroutine ODEINT, a Runge-Kutta method with adaptive stepwise control (see Numerical Recipes by Press et al. 2007, for details).

We assume that at the beginning of the observation the gas is in photoionization equilibrium with the ionizing continuum, and use the equilibrium concentrations as

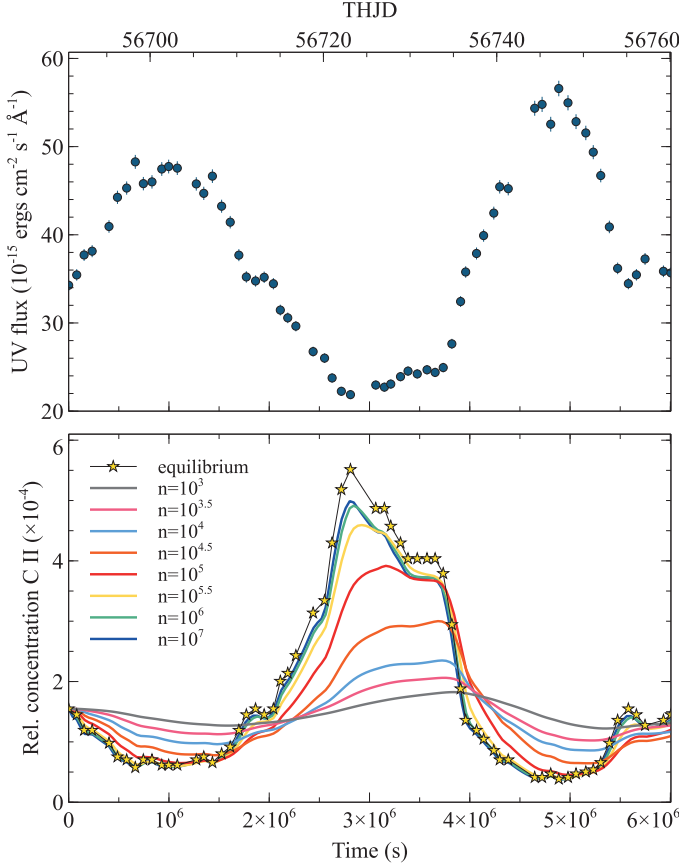


Figure 3.2: Time-dependent evolution of the relative concentrations of C II (1334 Å) (lower panel) responding to changes in the UV continuum as seen by HST at 1367 Å (upper panel), for different gas densities, n , in cm^3 . THJD refers to the Truncated Heliocentric Julian Date = (HJD-240000).

the initial conditions for the gas. The equilibrium concentrations are provided by CLOUDY when retrieving the ionization and recombination rates. Furthermore, we assume that the electron density, n_e , remains constant during the observation (following the same approach described in Nicastro et al. 1999; Arav et al. 2012; Kaastra et al. 2012; Silva et al. 2016). The time-dependent concentrations are then computed for a grid of gas densities, from 10^3 cm^{-3} up to 10^7 cm^{-3} , in 0.1 dex steps. Fig. 3.2 shows as an illustrative example the solutions obtained for C II (1334 Å).

The equilibrium concentrations are represented by the star markers in the lower panel of Fig. 3.2. These are the expected concentrations if the gas responds instantaneously to the changes in the continuum. As the flux increases, the relative concentration of C II is reduced, since the gas becomes more ionized. When the flux

drops, the gas recombines and the concentration of C II increases. The colored lines represent the predicted time-dependent ion concentrations for different gas densities. For high gas densities ($10^6 - 10^7 \text{ cm}^{-3}$), the gas response is close to what is expected from photoionization equilibrium. For low densities (e.g. 10^3 cm^{-3}), the gas is not able to respond to the flux variations. Instead, the concentration of C II varies slightly around a mean value, associated with the mean flux level over long timescales. Finally, for intermediate densities ($10^{4.5} - 10^{5.5} \text{ cm}^{-3}$), the gas response to the flux variations is a smoothed and delayed version of the light curve.

This response time of the gas is often associated with an equilibrium timescale from which an estimate of the density of the gas can be obtained (Krolik & Kriss 1995). In this work, we attempt to constrain the density of the absorbing gas by directly comparing the predicted changes of the ionic columns to the measured equivalent width light curves.

3.4 The density of the ionized absorber

In the optically thin limit, the curve of growth for the spectral lines shows a linear regime in which the equivalent width, EW , is directly proportional to the ionic columns, N_i . This linearity ensures the linear scaling of the equivalent widths with the predicted relative concentrations, n_{X^i} , given that the total column density of the gas does not change over the considered timescales. The linear scaling of these quantities allows for a direct comparison between the ion concentration curves we previously calculated with our time-dependent photoionization model and the light curves of the measured equivalent widths. Thus, the optically thin regime is of crucial importance for this approach. Once the gas becomes optically thick, and the lines become saturated, this linearity is no longer valid.

To determine which electron density predicts best the observed variations in the measured equivalent widths, we fit the predicted ion concentrations for the different densities to the light curves of each ion. The fitted model includes two free parameters; the scaling factor a_{X^i, n_e} and the offset b_{X^i, n_e} , which allow for the linear scaling relation between the measured equivalent widths and predicted ion concentrations, given by: $EW_{X^i, n_e}(t) = a_{X^i, n_e} n_{X^i, n_e}(t) + b_{X^i, n_e}$. The best fit is considered to be the curve that yields the lowest χ^2 , giving us a constraint on the electron density of the gas. For highly ionized plasmas, the density of the outflowing gas and the electron density are related by $n_e \simeq 1.2 n_H$. In this way, it is trivial to estimate from our results the density of the ionized gas, and in turn its distance to the central source. The distance is estimated through the definition of the ionization parameter, ξ , which depends on the ionizing luminosity, L_{ion} , the density of the gas, n_H , and its distance to the central source, r , and can be written as $\xi = L_{\text{ion}}/(n_H r^2)$.

3.4.1 Constraining the density of component 1

In Sec. 3.3, we calculated the predicted ion concentrations for component 1, using the ionization parameter estimated by Arav et al. (2015) as a proxy for the averaged ionization of the gas. We now fit the predicted ion concentrations for different densities (as a function of time), to the equivalent width light curves of the absorption troughs detected for this component of the UV outflow. The results of the best-fits are presented in Fig. 3.3, Fig. 3.4, and Table 3.1.

Here we consider C II to illustrate the results obtained for the behaviour of the EW as a function of time. In the upper-left panel of Fig. 3.3 the best-fit model for C II is plotted. It is first worth noting that by convention, the equivalent width measurements are negative since these relate to absorption lines. As seen in Fig. 3.2, a decrease in the ionizing flux leads to an increase in the concentration of C II due to radiative recombination, which translates into an increase in the absolute value of the measured equivalent width. For this reason, the scaling factor a_{X_i, n_e} is always negative throughout the fitting. The top-right panel in Fig. 3.3 shows the corresponding χ^2 values for the best-fit model for each density, in which the scaling factor a_{X_i, n_e} and the offset b_{X_i, n_e} parameters were free to vary. The density that best describes the behavior of the gas in these conditions is the density for which we obtain the best overall fit, i.e. the density whose best-fit model has the lowest χ^2 .

As shown in Fig. 3.3, Fig. 3.4, and Table 3.1, the density diagnostics through the study of these lines are robust and consistent with a density of $\log n_e \sim 4.9 - 5.0 \text{ cm}^{-3}$. Although the fitting results show good constraints on the density diagnostics for C II, Si II, and P V, the lowest χ^2 achieved yields a $\chi_{\text{red}}^2 < 1$. A $\chi_{\text{red}}^2 < 1$ is a problem we encounter for some of our fits. This indicates that the error variance is likely to be over-estimated, i.e. that the estimated uncertainties on the EW s (see Sec. 3.2) may be in some cases too conservative. To account for this, we scale the χ^2 values of the fits that originally yield a $\chi_{\text{red}}^2 < 1$, by setting the achieved χ_{min}^2 to the number of *d.o.f.*, such that the best fit returns $\chi_{\text{red}}^2 = 1$. This mostly affects the uncertainties of the fitted parameters, since the estimated errors after scaling are larger, hence more conservative (see the values in brackets on Table 3.1). The best-fits for C II, Si II, and P V are less constraining when correcting for the over-estimation of the error variance in the fits. Computing the errors in $\log n_e$ by scaling the χ^2 so that the minimum corresponds to a $\chi_{\text{red}}^2 = 1$, results in $\log n_e > 3.3 \text{ cm}^{-3}$ for C II, $\log n_e > 4.1 \text{ cm}^{-3}$ for Si II, and $\log n_e \sim 4.9^{+0.8}_{-0.6} \text{ cm}^{-3}$ for P V. The fitting results for component 1, using the best estimates for the lines providing tighter constraints, Si III and Si IV, yield $\log n_e \sim 4.9 - 5.0 \text{ cm}^{-3}$, which corresponds to a gas number density in the range of $n_{\text{H}} \sim (6.6 - 8.3) \times 10^4 \text{ cm}^{-3}$. We note however that given the close agreement in fit parameters, the rescaling of the χ^2 values for the fits of the lines of C II, Si II, and P V may not be required. Nonetheless, we present this conservative resulting confidence intervals, for completeness.

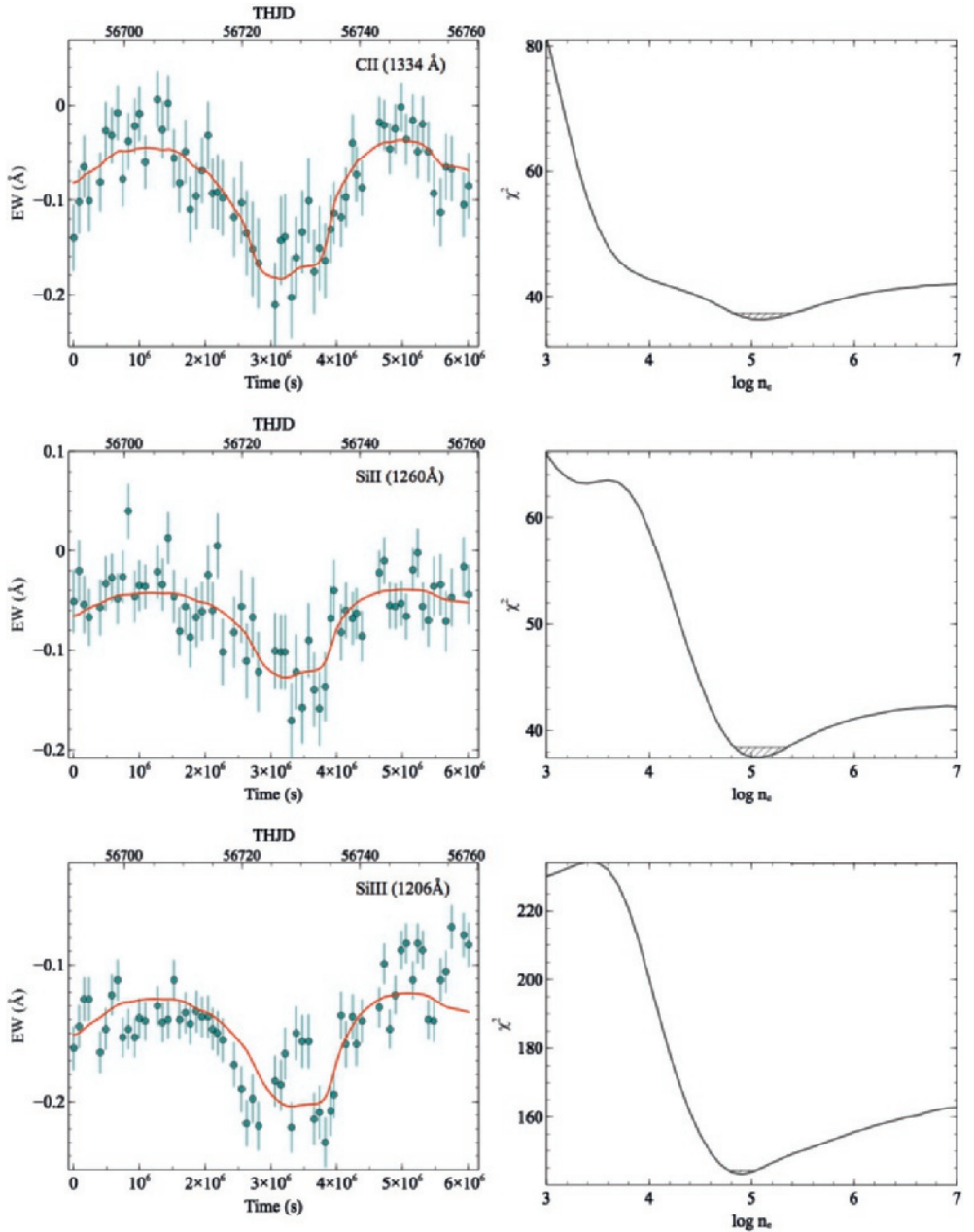


Figure 3.3: Best fits for component 1. The plots on the left show the C II, Si II, and Si III EW light curves and the corresponding best-fit model to each one of these lines. The plots on the right show the corresponding χ^2 values for the best-fit model for each density. The 1σ region of confidence, is represented by the dashed area in the curves.

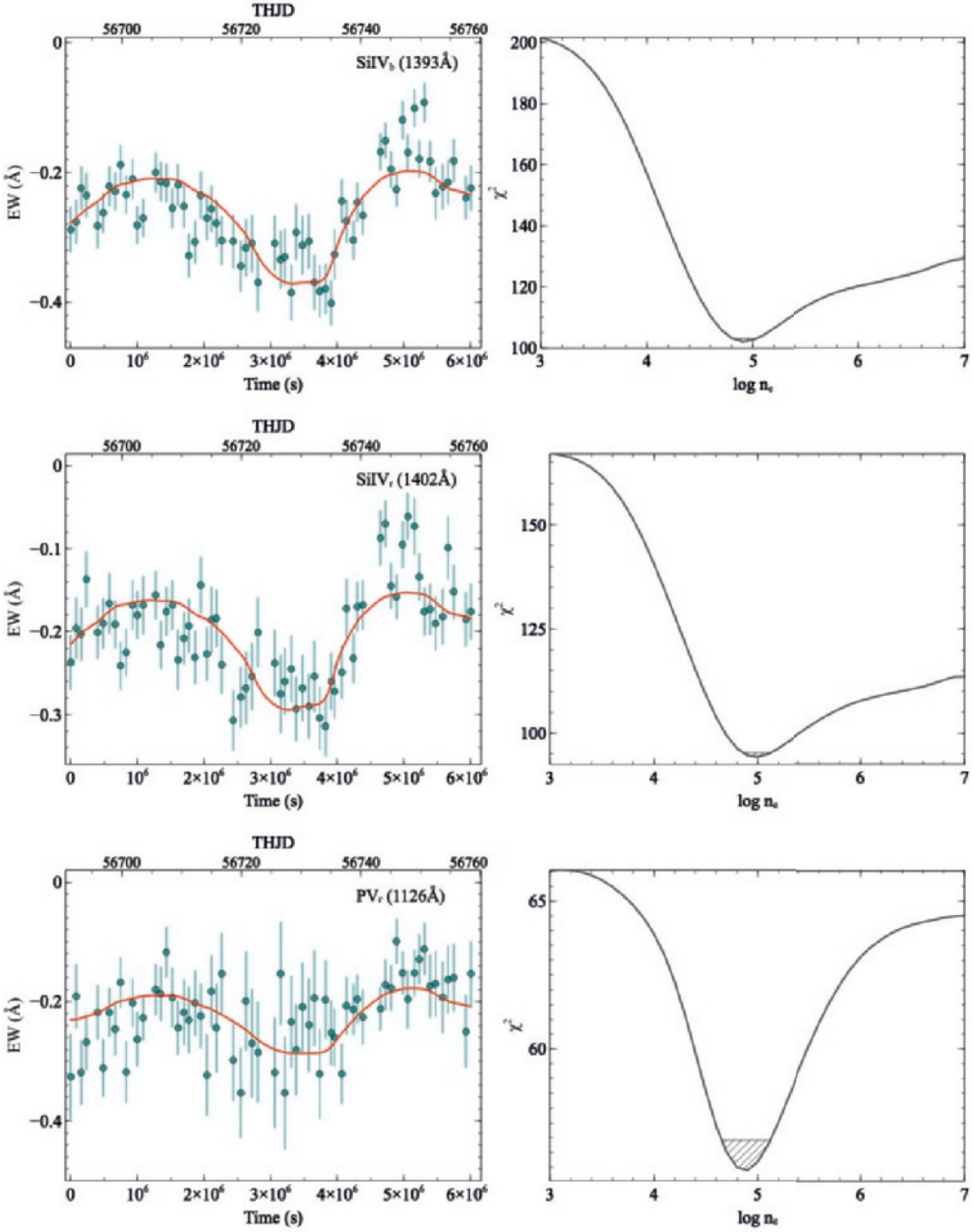


Figure 3.4: Best fits for component 1. The plots on the left show the Si IV_b and P V_r EW light curves and the corresponding best-fit model to each one of these lines. The plots on the right show the corresponding χ^2 values for the best-fit model for each density. The 1σ region of confidence, is represented by the dashed area in the curves. The indexes r and b respectively refer to red and blue transitions for doublets.

Table 3.1: Results of the best fits for component 1. 1σ errors, equivalent to 68% confidence level, are estimated by taking the corresponding $\Delta\chi$ value for one parameter of interest, $\Delta\chi = 1.0$. *The errors on the estimated number density for the fits of C II, Si II and P V have also been computed by correcting for the over-estimation of the error variance in our fits (in brackets).

| Absorption line | $\log n_e$ (cm^{-3}) | $\chi^2/d.o.f.$ |
|-----------------------------|---|-----------------------|
| C II (1334 Å) | $5.1^{+0.1}_{-0.2} (> 3.3)^*$ | 36.34/59 \sim 0.62 |
| Si II (1260 Å) | $5.0^{+0.2}_{-0.1} (> 4.1)^*$ | 37.48/58 \sim 0.65 |
| Si III (1206 Å) | 4.9 ± 0.1 | 143.31/61 \sim 2.3 |
| Si IV _b (1393 Å) | 4.9 ± 0.1 | 102.09/61 \sim 1.67 |
| Si IV _r (1402 Å) | 5.0 ± 0.1 | 94.31/61 \sim 1.54 |
| P V _r (1126 Å) | $4.9^{+0.2}_{-0.1} (4.9^{+0.8}_{-0.6})^*$ | 55.90/61 \sim 0.92 |

In addition to the aforementioned Si II λ 1260Å absorption trough, it was also possible to retrieve for component 1 the *EW* light curves of Si II λ 1193Å, Si II λ 1304Å and Si II λ 1526Å. Variations in these troughs are small in amplitude and additionally affected by a low signal-to-noise ratio. Consequently, the fits to these absorption troughs of Si II provide, at most, lower limits on the number density (see Fig. A.1). Troughs of Al II and S III were also observed. The *EW* light curves of these lines suffer particularly from this signal-to-noise ratio problem in a way that has led these lines to be unusable as a diagnostic on their own (see Fig. A.2). Finally, prominent lines of Ly α , C IV and N V are also present in the spectra. The absorption troughs of Ly α , C IV and N V are much stronger, showing rapid variations of much higher amplitude than any of the other troughs (see Fig. A.3). While the long term changes in these lines correlate with the continuum, the rapid and high amplitude variability of the *EW* light curves cannot be described by a simple photoionization model. For this reason, these lines will not be included in the subsequent analysis throughout this paper. In Sec. 3.5, we discuss possible scenarios that can account for this complex behaviour.

3.4.2 Constraining the density and ionization of the UV absorber

The previous analysis relied on prior knowledge of the ionization state of the gas. In the UV, constraining the gas ionization is not trivial due to the low number of transitions available for a diagnostic. Out of the six outflow components identified in the spectra of NGC 5548 it was only possible to constrain the ionization of the gas for component 1 (Arav et al. 2015). In the light of this, we have extended our models to allow for a range of ionization parameters, enabling us to simultaneously constrain

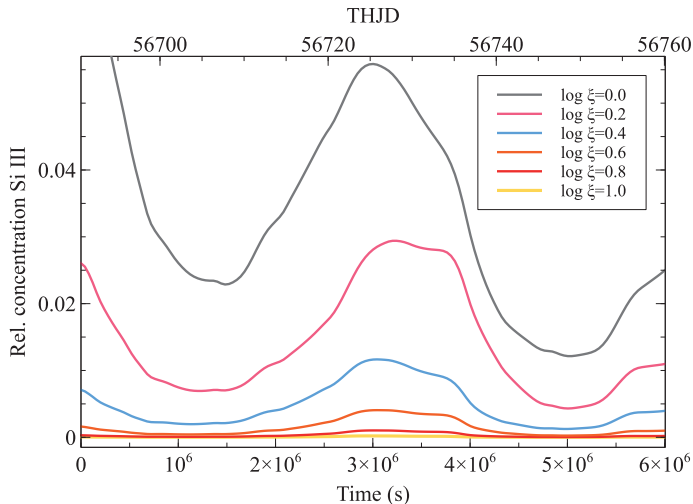


Figure 3.5: Time-dependent evolution of the relative concentrations of Si III (λ 1206Å) responding to changes in the UV continuum (see upper panel in Fig. 3.2) for different ionization states, at a fixed density of $\log n_e = 5.0$.

the density and ionization state of the gas.

Different ionization states also have an impact on the time-dependent evolution of the ion concentrations. An illustrative example is presented in Fig. 3.5, where the time-dependent ion concentrations of Si III are plotted for a range of ionization parameters ($\log \xi = 0.0 - \log \xi = 1.0$), at a fixed density of $\log n_e = 5.0 \text{ cm}^{-3}$. While the biggest effect of ionization is on the relative abundance of the different ions, changes in the shape of the curves are also noticeable even when considering a fixed density. Thus, in addition to being sensitive to the density, we expect the modeling to be sensitive to ionization.

The different absorption troughs of each kinematic component are assumed here to be part of the same gas phase, sharing the same physical conditions, i.e. same ionization state and density. As we have seen in our previous fits to the absorption troughs of component 1, the results for the different lines for which we obtain good fits are consistent with one another. Since one extra parameter is here added to our model, a stronger constraint is given by fitting together the lines corresponding to each component. Thus, we perform a joint-fit for each component in order to find the its best fitting density and ionization parameter, in a consistent manner.

The predicted ion concentrations are first calculated in a similar fashion to what is described in Sec. 3.3, only this time the CLOUDY runs are also performed over a range of ionization parameters. Based on the results we achieved for component 1, we consider a narrower density range from $\log n = 4.0 \text{ cm}^{-3}$ up to $\log n = 6.0$

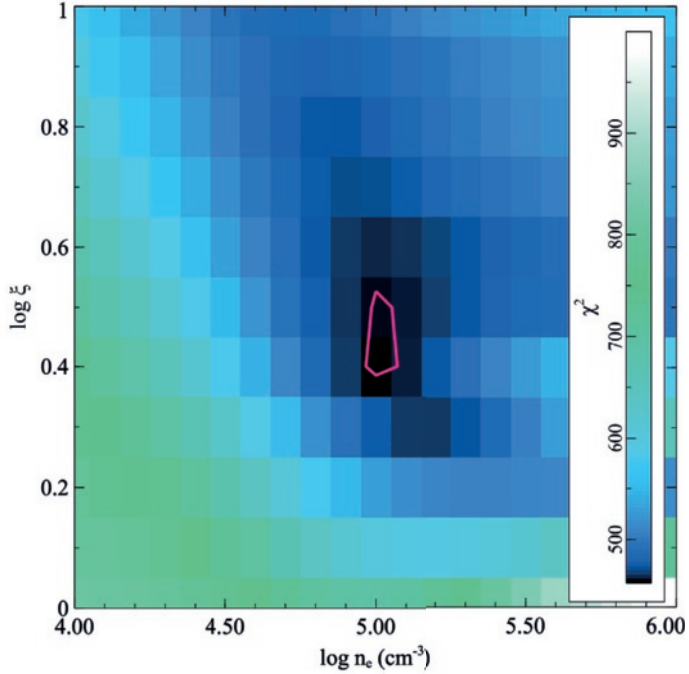


Figure 3.6: Contours for the joint fit of component 1 including C II, Si II λ 1260Å, Si III, Si IV, and P V. The 1σ region of confidence (for 68% significance level), is represented by the solid line in magenta.

cm^{-3} , and a ionization parameter $\log \xi$ in between $\log \xi = 0.0$ and $\log \xi = 1.0$, both in a grid of steps of 0.1. These models are fitted to the equivalent width light curves as before, including the two free parameters $a_{X_{i,n_e}}$ and $b_{X_{i,n_e}}$. The joint fit is achieved by performing a 2-dimensional grid search across these ranges of ionization parameters and densities. The pair (n_e, ξ) that best predicts the observed changes in the measured equivalent widths is the one that yields the overall lowest χ^2 , when the results of the grid search for each absorption line are computed together.

Component 1

For component 1 we successfully constrained the density of the gas through the modeling of the absorption troughs of C II, Si II λ 1260Å, Si III, Si IV, and P V (see Sec. 3.4.1), while making use of the averaged ionization state found for this component by Arav et al. (2015). Combining the fits to the aforementioned absorption troughs, we now perform a joint fit to simultaneously constrain the ionization and density of this gas component. A minimum χ^2 estimation is first computed for each line. Subsequently, we correct the results obtained for which the χ^2_{\min} is lower than the number

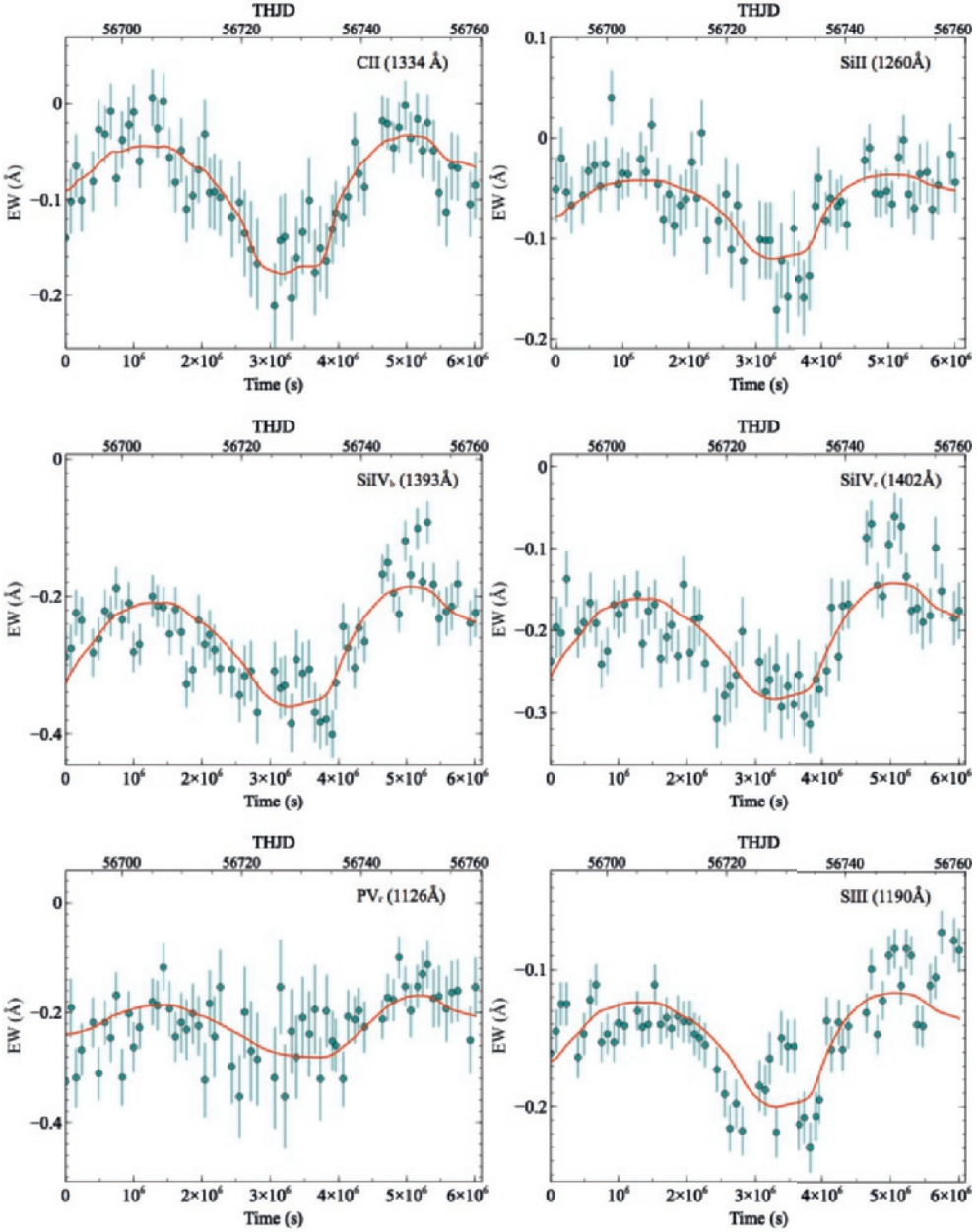


Figure 3.7: Best fit models for the joint fit of component 1 including C II, Si II (λ 1260Å), Si III, Si IV, and P v. The indexes r and b respectively refer to red and blue transitions for doublets.

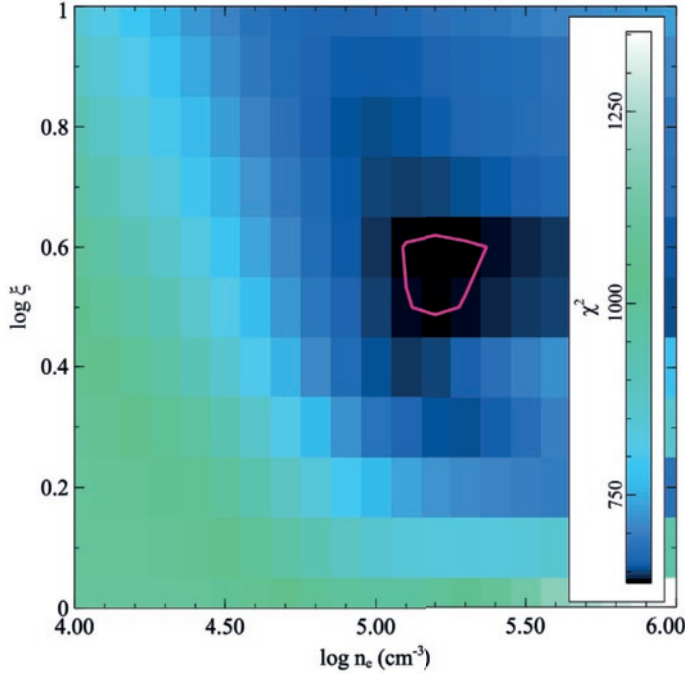


Figure 3.8: Contours for the joint fit of component 1 including C II, Al II, Si II, Si III, Si IV, P V, and S III. The 1σ region of confidence (for 68% significance level), is represented by the solid line in magenta.

of *d.o.f.*, yielding a $\chi_{\text{red}}^2 < 1$, as it was the case for C II and P V. As mentioned earlier this yields a conservative approach to the estimation of the uncertainties on the fitted parameters. The results of the 2-dimensional grid search for each trough are summed, according to the additive properties of the χ^2 distribution, and the (n_e, ξ) pair corresponding to the lowest total χ^2 are considered the best-fit parameters. To estimate the confidence limits on these parameters, we find the 1σ region of confidence (for 68% significance level), for two parameters of interest (i.e. $\Delta\chi = 2.3$), and interpolate on the grid of n_e and ξ to retrieve the errors. The parameters that predict best the observed changes in the measured equivalent widths are $\log n_e \sim 5.00^{+0.08}_{-0.05}$ and $\log \xi \sim 0.40^{+0.05}_{-0.10}$ with $\chi^2/d.o.f. = 457/361 \sim 1.27$. The contours of the joint fit are presented in Fig. 3.8, and the results of the joint fit are shown for each line in Fig. 3.7.

We further set out to constrain the density and ionization of the gas by also making use of the *EW* light curves showing lower signal-to-noise ratios, namely Al II, the remaining lines of Si II, and S III. A joint fit including these troughs in addition to the troughs previously mentioned resulted in $\log n_e \sim 5.20^{+0.17}_{-0.10}$ and $\log \xi \sim 0.50^{+0.12}_{-0.03}$

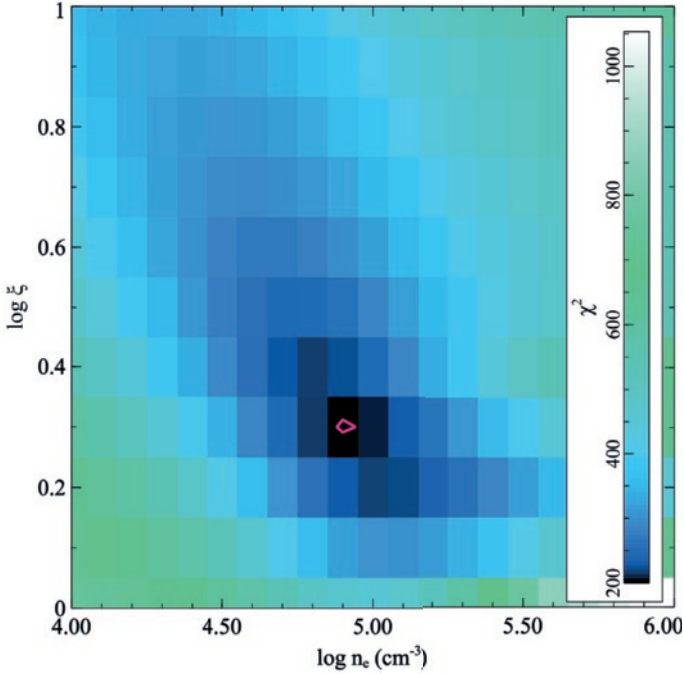


Figure 3.9: Contours for the joint fit of component 3. The 1σ region of confidence (for 68% significance level), is represented by the solid line in magenta.

with $\chi^2/d.o.f. = 816/615 \sim 1.33$. The contour plot of the joint fit involving all these lines is shown in Fig. 3.8, and Figs. A.4 and A.5 show the results of the joint fit for each of the lines.

Component 3

Component 3 shows variations in the troughs of Si III and Si IV. A joint fit to the equivalent width lightcurves of these absorption lines yields remarkable constraints of the physical parameters of this component, with $\log n_e \sim 4.90^{+0.05}_{-0.03}$ and $\log \xi \sim 0.30 \pm 0.02$ with $\chi^2/d.o.f. = 200/177 \sim 1.13$. The contour plot of the joint fit for component 3 is presented in Fig. 3.9. Fig. 3.10 shows the results of the joint fit to each one of the studied lines. The density of component 3 is comparable to the density of component 1, within the errors. Our results however point to a lower ionization in component 3 compared to component 1, suggesting component 3 to be located further from the central source than component 1.

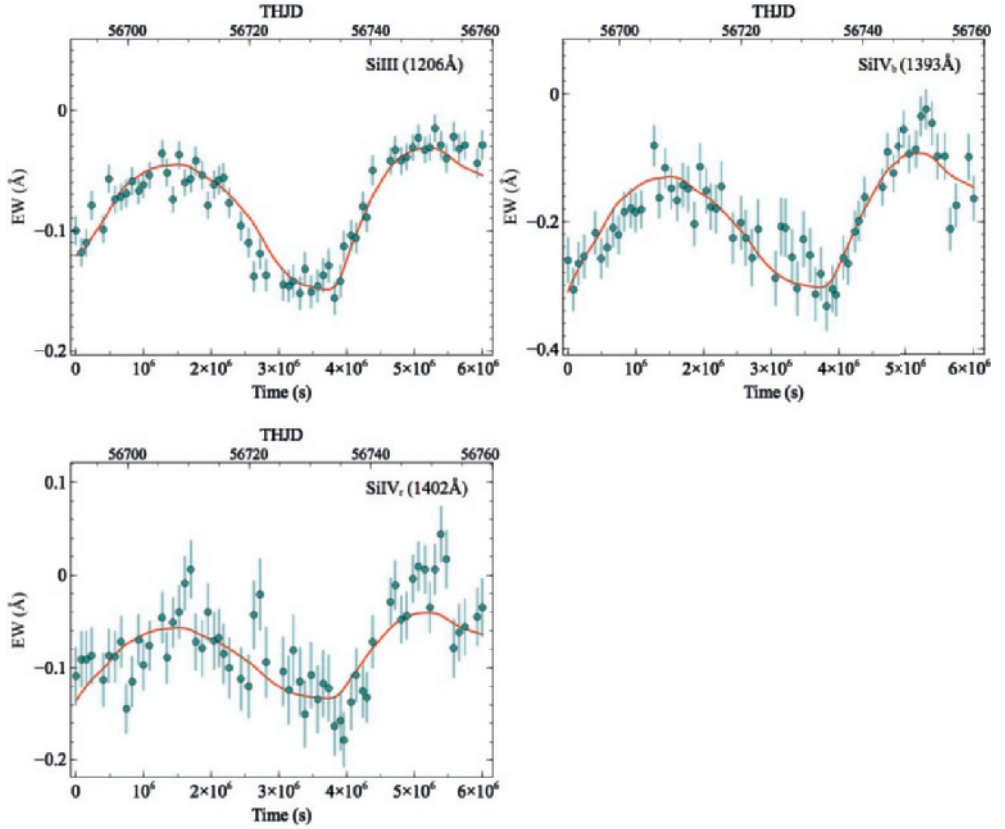


Figure 3.10: Best fit models for the joint fit of component 3 including Si III and Si IV. The indexes r and b respectively refer to red and blue transitions for doublets.

Components 2, 4, 5 & 6

It is not possible to set constraints on the parameters of the remaining kinematic components observed in the spectra of NGC 5548. Component 2 only shows variations in the troughs of Ly α , C IV and N V, for which we are not able to successfully apply our model due to the complexity of these features (see Fig. A.6). Troughs of Si IV are detected for component 4, however these do not show any variations across the length of the observation period we consider (see Fig. A.8). The lack of variability can be explained by very low gas densities, or can imply a distant location of the gas from the ionizing source, as inferred by Arav et al. (2015). The same is true for components 5 and 6, for which no significant variability is detected during the considered time-scale for the troughs of Si III and Si IV (see Figs. A.9 and A.10). Interestingly, all these components show variability in the troughs of Ly α , C IV and N V.

3.5 Discussion

By expanding on the time-dependent photoionization model developed by Silva et al. (2016), we have calculated the behaviour of the relative ion concentrations, as a function of time, for the narrow absorption troughs present in the spectra of NGC 5548. The changes over time, considered in our model, are solely due to photoionization and radiative recombination, as a result of the variability of the ionizing continuum. The high-quality data of this campaign allows for the time-dependent response of the gas to be observed in remarkable detail, by measuring the changes in the EW of the troughs on timescales of ~ 1 day, over a period of roughly 6 months. As explained earlier in Sec. 3.3, in this work we only make use of the data taken during the first part of the campaign, roughly corresponding to the first 60 days of observations, where the changes in the lines are seen to correlate with the changes in the continuum. This provides exceptional conditions to test our method, since during this time, the narrow absorption lines show the classic behavior expected from photoionization. During the second half of the campaign, the lines show an anomalous behaviour likely due to changes in the shape of the underlying SED (Goad et al. 2016; Mathur et al. 2017); their analysis is out of the scope of this paper.

By fitting the predicted ion concentrations to the EW light curves, we successfully determine the density and ionization states of components 1 and 3. We first constrain the density of component 1 to be $n_e \sim 4.9 - 5.0 \text{ cm}^{-3}$, for the assumed ionization parameter inferred for this component by Arav et al. (2015), $U \sim -1.5$ which corresponds to $\xi \sim 0.69$ for the considered SED. The density of the outflowing gas and the electron density are related by $n_e \simeq 1.2 n_H$, for highly ionized plasmas. Thus the electron density we estimated corresponds to a gas number density in the range of $n_H \sim (6.6 - 8.3) \times 10^4 \text{ cm}^{-3}$. These results are consistent with the values estimated by Arav et al. (2015), using the metastable levels of the absorption troughs of C III* and Si III*. These estimates place the outflowing gas at a distance of 2.5-2.8 pc from the central source, well within the estimated size of the narrow-line-emitting region in this source (Peterson et al. 2013).

In the second part of our analysis, we simultaneously, and in a consistent manner, constrain the density and ionization parameter of the gas by performing a joint fit of the corresponding lines for each component, for a grid of gas densities and ionization parameters. The results of these fits are remarkable. Both the density and the ionization parameter of the gas are determined to a high accuracy. For component 1, we find $\log n_e \sim 5.00_{-0.05}^{+0.08}$ and $\log \xi \sim 0.40_{-0.10}^{+0.05}$. These results point to a slightly lower ionization state when compared to the estimates from Arav et al. (2015), however the constraints on the density are still consistent. This highlights how the shape of variations is primarily influenced by the density of the gas. The time-dependence of the gas is nonetheless also sensitive to the subtle differences between the ionization states allowing for this parameter to also be inferred from our models. For compo-

nent 3, we obtain $\log n_e \sim 4.90_{-0.03}^{+0.05}$ and $\log \xi \sim 0.30 \pm 0.02$. Within the errors, the density of component 3 is comparable to the density of component 1. The ionization parameter of component 3 though is lower than what we found for component 1. This suggests that component 3 is likely to be located farther from the central source than component 1. A larger radial distance was also suggested for component 3 in the analysis of Arav et al. (2015), who found this gas phase to likely be located at $5 < R < 15$ pc. Our estimates however would place this kinematic component at a distance of ~ 3.5 pc from the central source. This discrepancy is mainly due to the fact that our fits indicate a higher density than the density range estimated by Arav et al. (2015), which naturally implies a smaller radial distance, even though the ionization parameter we find is slightly lower than what it is assumed in their work.

Despite the good results obtained from our fits, we find that there are some clear residuals towards the end of the first part of the observations that are worth discussing. This particularly regards the best-fits of Si III and Si IV, see e.g. Fig 3.7. The equivalent width of these lines during this period shows a decrease that our model alone is not able to explain. Mathur et al. (2017) found an excess of flux in soft X-rays to occur around the same time, suggesting a change on the underlying ionizing spectral shape. These changes were pointed out as the likely cause for the anomalies observed in the emission lines, which after this period, appear to be uncorrelated with the continuum (Goad et al. 2016). Since our model predicts the variations of these lines based on the variability of the UV light curve alone, it is not surprising that it will not account for an unexpected change in the underlying spectral shape of the ionizing continuum, which naturally will affect the behavior of the lines.

The success of our method is demonstrated by the notable results achieved for components 1 and 3. Its validity, however, is dependent on certain conditions. To start with, variability studies of this kind require high-quality data where the source is continuously monitored, over a long period of time. To date, such comprehensive campaigns are rather uncommon, making these UV observations of NGC 5548 somewhat exceptional. The physical properties of the outflowing gas also play a role here. Low density gas, or gas located at large radial distances from the central source, is predominantly affected by large amplitude variations in the illuminating continuum over long timescales, and response times in these cases may also be long. This is likely to be the situation for components 2, 4, 5, and 6, which do not show variability over the considered timescales for the troughs that would yield a diagnostic, such as Si III and Si IV. Finally, this method is only valid in the optically thin limit. Only in this case, is it possible to compare the variations in the EW of the lines to the predicted ion concentrations, since the EW variations in this regime are directly proportional to the ionic columns. For saturated lines, the relation between the ionic columns and the equivalent width is non-linear and therefore, we do not expect the equivalent width

changes to be well modeled by the ionic columns. The absorbing gas in NGC 5548 shows prominent lines of Ly α , C IV and N V. These troughs vary widely over time. Such variations do correlate with the continuum variability, however their behavior is much more complex than what we find for the troughs of lower ionization lines (e.g. C II) and a good fit cannot be found with our model. From their analysis, Arav et al. (2015) have indicated that the absorption troughs of Ly α , C IV and N V are likely to be highly saturated. This likely explains why our model is not suitable for the modelling of these troughs. On the other hand, if the geometry of the gas is more complex than expected (e.g. if the outflow is not homogeneous), its response to changes in the continuum will also be more complex. A possibility is that the absorbing clouds with strong Ly α , C IV and N V are stratified in density, and possibly self-shielding to some extent. The low-ionization lines, in this case, arise in the cool, dense core, while the higher-ionization ions are created over a much large volume. Most of that volume produces saturated high-ionization lines, but becomes more optically thin on its outer boundaries. These optically thin layers could then produce the variations we see in the Ly α , C IV and N V lines, which appear only in the wings of their line profiles and not in the saturated core. Our model, which considers an homogeneous layer of gas responding to variations in the ionizing flux, may be oversimplified in these cases.

3.6 Conclusions

Using a time-dependent photoionization model, we numerically computed the time-dependent ion concentrations of several atomic species present in ionized outflow of NGC 5548, as they respond to changes in the ionizing continuum. The predicted ion concentrations are compared to the light curves of the measured equivalent widths, yielding an estimate for the density, and hence distance, of the gas. Our findings can be summarized as follows:

1. A simple photoionization model, which predicts the time-evolution of the ion concentrations simply due to the variability of the central source, is able to explain the variations in the measured equivalent widths of the absorption lines over time.
2. Given the ionization parameter estimated by Arav et al. (2015), we were able to obtain the density of component 1, by comparing the predicted time-dependent ion concentrations, for a grid of densities, to the equivalent width light curves of C II, Si II, Si III, Si IV, and S III. The estimates on the density from the different troughs are consistent, yielding $n_{\text{H}} \sim (6.6 - 8.3) \times 10^4 \text{cm}^{-3}$, from which a radial distance of 2.5-2.8 pc could be inferred. These estimates place this component well within the estimated size for the narrow-line-emitting region in this source.

3. By expanding our models to allow for a range of ionization states, in addition to a range of gas densities, we are able to constrain the density and ionization state of components 1 and 3. We do so by performing a joint fit for the absorption troughs of each component. Our estimates allow us to infer the location of component 3 to be at ~ 3.5 pc from the central source.
4. The time-dependent behaviour of Ly α , C IV and N V cannot be explained with our simple model. This is likely due to a more complex geometry of the absorbing clouds where these high ionization troughs originate.
5. Time-dependent photoionization models are a powerful tool to study the complex behaviour of ionized absorption. High-resolution data and extensive observations of nearby sources are key to unveil in detail the processes at play and the physical parameters necessary to understand the nature, and characterize the importance of AGN outflows at large.